

DOI: 10.1002/((please add manuscript number))

**Article type: Communication**

**The Dynamic Mechanical Properties of Lead-Halide Perovskite Single Crystals are Independent of A-site Cation Chemistry**

*Marcos A. Reyes-Martinez, Ahmed L. Abdelhady, Makhsud I. Saidaminov, Duck Young Chung, Osman M. Bakr, Mercuri G. Kanatzidis, Wole O. Soboyejo and Yueh-Lin Loo\**

Dr. Marcos A. Reyes-Martinez  
Department of Chemical and Biological Engineering,  
Princeton University, Princeton, NJ 08544, USA

Prof. Yueh-Lin Loo  
Department of Chemical and Biological Engineering, and  
Andlinger Center for Energy and the Environment  
Princeton University, Princeton, NJ 08544, USA  
E-mail: lloo@princeton.edu

Dr. Ahmed L. Abdelhady, Dr. Makhsud I. Saidaminov, Prof. Osman M. Bakr  
Department of Materials Science and Engineering,  
King Abdullah University of Science and Technology (KAUST), Thuwal 23955-6900, Saudi Arabia

Dr. Duck Young Chung  
Materials Science Division, Argonne National Laboratory, Argonne, IL 60439, USA

Prof. Mercuri G. Kanatzidis  
Department of Chemistry, Northwestern University, Evanston, IL 60208, USA and  
Materials Science Division, Argonne National Laboratory, Argonne, IL 60439, USA

Prof. Wole Soboyejo  
Department of Mechanical and Aerospace Engineering,  
Princeton University, Princeton, NJ 08544, USA  
Present address: Department of Mechanical Engineering, Worcester Polytechnic Institute,  
Worcester, MA 01609, USA

Keywords: viscoplasticity, hybrid perovskites single crystals, nanoindentation, dynamic mechanical behavior

**The ease of processing hybrid organic-inorganic perovskite (HOIPs) films, belonging to a material class with composition  $ABX_3$ , from solution and at mild temperatures promises the use of their unique optoelectronic properties in deformable technologies, including flexible photovoltaic devices, sensors, and displays. To successfully apply these**

**materials in deformable devices, knowledge of their mechanical response to dynamic strain is necessary. We elucidate the time- and rate-dependent mechanical properties of HOIPs and an inorganic perovskite (IP) single crystal by measuring nanoindentation creep and stress relaxation. The observation of pop-in events and slip bands on the surface of the indented crystals demonstrate dislocation-mediated plastic deformation. The magnitudes of creep and relaxation of both HOIPs and IPs are similar, negating prior hypothesis that the presence of organic A-site cations alters the mechanical response of these materials. Moreover, these samples exhibit a pronounced increase in creep, and stress relaxation as a function of indentation rate whose magnitudes reflect differences in the rates of nucleation and propagation of dislocations within the crystal structures of HOIPs and IP. This contribution provides understanding that is critical for designing perovskite devices capable of withstanding mechanical deformations.**

Hybrid organic-inorganic perovskites (HOIPs) are a class of materials that continue to revolutionize the field of photovoltaics with devices now exhibiting power-conversion efficiencies in excess of 20%.<sup>[1-3]</sup> HOIPs belong to a wider class of materials with composition  $ABX_3$  where, the A cation is caged inside of a B-X framework. Most of the work on perovskite materials for potential photovoltaic applications has focused on materials with  $A = CH_3NH_3^+$  or  $Cs^+$ ;  $B = Pb^{2+}$ ;  $X = I^-$  or  $Br^-$ ,<sup>[4-9]</sup> with devices having  $CH_3NH_3PbI_3$  active layers holding record-breaking photovoltaic device performances.<sup>[3]</sup> The ease of processing of HOIPs from solution brings the promise of their application in thin-film devices beyond photovoltaics for deformable electronic technologies, including flexible electronics and other strain-intensive applications.<sup>[10]</sup> Researchers hypothesize that the rotational degrees of freedom of organic cations inside the Pb-X cage impart a “soft” character to HOIPs.<sup>[11]</sup> Nevertheless, the reported Young’s modulus and hardness, which quantify the resistance to plastic deformation for  $MAPbBr_3$  and  $CsPbBr_3$ , are similar in magnitude.<sup>[12]</sup> Therefore, it is

important to understand under what conditions the presence of an organic cation affects the mechanical behavior of HOIPs.

A few recent studies have characterized the static mechanical properties of lead-halide perovskites. Cheetham and coworkers<sup>[13]</sup> used nanoindentation to measure the Young's moduli and hardness of  $\text{CH}_3\text{NH}_3\text{PbX}_3$  ( $X = \text{I}, \text{Br}$  and  $\text{Cl}$ ) single crystals. They attributed differences in elastic properties to differences in Pb-X framework. Cahen and coworkers<sup>[12]</sup> also conducted nanoindentation studies on single crystals of  $\text{CH}_3\text{NH}_3\text{PbX}_3$  ( $X = \text{I}$  and  $\text{Br}$ ), with the addition of the all-inorganic  $\text{CsPbBr}_3$ , and reached similar conclusions as Cheetham. Feng<sup>[14]</sup> used DFT to calculate the elastic constants of  $\text{CH}_3\text{NH}_3\text{BX}_3$  where  $B = \text{Sn}, \text{Pb}$  and  $X = \text{Br}, \text{I}$ . The computed Young's moduli (uniaxial deformation), shear moduli (shearing or torsional deformation), and bulk moduli (uniform compression) are in qualitative agreement with experimental measurements. The ductility index (bulk-to-shear modulus ratio,  $B/G$ ) for the cubic, tetragonal and orthorhombic phases of each material, were uniformly greater than 1.75; suggesting that these materials are all highly ductile.

Although the ability of HOIPs to deform plastically has been predicted by their low bulk-to-shear modulus ratio<sup>[14]</sup> and low hardness,<sup>[12,13]</sup> the dynamics of plastic deformation have not been characterized. Time-dependent mechanical measurements, such as creep and stress relaxation, lend insights to strain hardening and response time of these materials under constant mechanical load/deformations and their response with different rates of deformation. Such dynamic mechanical response is crucial to the design of device architectures for strain-intensive applications and sheds light on the limitations they will have in large-scale processing where varying degrees of deformation might be experienced (i.e., roll-to-roll). Also, knowledge of both static and dynamic mechanical properties will allow for new structure-property correlations to be established.

Here we utilize nanoindentation creep and stress relaxation measurements to demonstrate pronounced rate-dependent inelastic mechanical behavior (viscoplasticity) in bulk single

crystals of lead-halide perovskites with both organic and inorganic cations. We focused our study on single crystals of three perovskite compositions: methylammonium lead bromide ( $\text{MAPbBr}_3$ ), methylammonium lead iodide ( $\text{MAPbI}_3$ ), and an all-inorganic perovskite of cesium lead bromide ( $\text{CsPbBr}_3$ ). As a reference material for comparison, we measured the mechanical response of an ionic single crystal, potassium bromide ( $\text{KBr}$ ).  $\text{KBr}$  was chosen since it is a well-known, commercially available ionic crystal, with a crystal structure different from that of  $\text{ABX}_3$  and has well characterized mechanical properties,<sup>[15]</sup> including low hardness ( $H = 0.15$  GPa). Contrary to conventional wisdom, our measurements suggest that the time-dependent mechanical response of the inorganic-organic perovskite is independent of the chemical character of the A-site cation. We utilize the discontinuities in load-penetration curves, also known as pop-in events, to characterize differences of elastic-to-plastic transitions in  $\text{MAPbBr}_3$ ,  $\text{MAPbI}_3$ ,  $\text{CsPbBr}_3$  and  $\text{KBr}$  single crystals. The differences between the creep and load relaxation curves (obtained from the materials tested in this study) are attributed to dislocations phenomena that occur during the nanoindentation experiments. Finally, we use a viscoplastic constitutive equation derived from a rheological model to fit the experimental data. The implications of the results are discussed for potential application of perovskites in flexible electronic devices.

In all experiments, we indented one facet of each crystal.  $\text{MAPbBr}_3$ ,  $\text{MAPbI}_3$ , and  $\text{KBr}$  were indented on their (100) planes. Due to the preparation of the  $\text{CsPbBr}_3$  crystal,<sup>[16]</sup> we were only able to indent in the direction normal to a face preferentially oriented on the (200) plane. X-ray diffraction pattern for  $\text{CsPbBr}_3$  crystal is shown in Figure S1. Unit cell and structural parameters, as well as photographs of the crystals tested are shown in Table S1.

We conducted nanoindentation experiments in load-controlled (**Figure 1a**) and displacement-controlled (**Figure 1b**) modes. These were used, respectively, to study creep and stress relaxation. Holding the load fixed during nanoindentation for a period of time allows us to record the displacement into the sample. Similarly, holding the displacement fixed

allows us to monitor the load relaxation. From these experiments, we compared the time-dependent mechanical response of HOIPs and inorganic perovskites to obtain new insights about the dynamic mechanical behaviors of these materials. Figure 1c shows a plot of creep against time. All the curves display a steep initial creep followed by a reduction in the rate of penetration. Interestingly, both hybrid and inorganic perovskite materials exhibit large creep displacements compared to KBr. Figure 1d shows plots of load relaxation versus time, for all the materials that were tested. Similar to the creep displacement plots, KBr shows the least load relaxation over time. Moreover, the magnitude of the relaxation by the hybrid and inorganic perovskites is similar, suggesting that the organic cation is not unique in affecting the dynamic mechanical response of the indented single crystals. Previous work in Pb-based HOIPs showed that the strength of the Pb-X bond dominates the elastic response of the material.<sup>[12-14]</sup> Our results imply that the Pb-X framework may also dominate the viscoplastic behavior.

It is well known that nanoindentation nucleates and propagates dislocations in crystalline samples,<sup>[17-19]</sup> causing plastic deformation. Quantitative evidence of plastic deformation is observed in discontinuities in displacement, known as pop-in events (Figure 2a). Pop-in events occur when the stresses under the indenter tip reach critical levels that are sufficient for the nucleation and propagation of slip dislocations. Scanning electron micrographs of indents offer evidence for slip-mediated plastic deformation through the presence of shear bands (Figure 2b) on the surface of the crystal.<sup>[20,21]</sup> To characterize the differences in slip activation in the single crystals, we analyzed how the pop-in displacement depends on pop-in load in Figure 2c. The change in indentation depth as a function of load during pop-in events is attributed to the nucleation of dislocations.<sup>[22]</sup> We observed that the inverse of individual slopes (pop-in load/pop-in extension) scale with hardness, indicating that the hardness of the crystals tested is directly proportional to the critical condition for dislocation nucleation (Figure 2d). Interestingly, the hardness alone does not give any insight to the large differences

in creep and relaxation characteristics between KBr and the materials with perovskite structure. Hence, to explain the large differences between the time-dependent behavior of perovskite materials and KBr, we explore the differences in the dynamics of plastic deformation.

Since the deformation that occurs in the crystals during nanoindentation can nucleate dislocations, the slowdown in the rate of penetration observed in Figure 1c is consistent with strain hardening. Strain hardening is the increased resistance to plastic deformation that occurs as a consequence of the interactions of dislocations.<sup>[23,24]</sup> To further explore, we performed two consecutive creep experiments on the same area of MAPbI<sub>3</sub> single crystals (Figure S3). When comparing the creep behavior of the first and second measurements, a significant reduction of displacement is observed on the subsequent creep experiment. The reduced displacement is evidence for higher resistance to plastic deformation, quantified by an increase in hardness ( $H = P_{max}/A$ ) from 0.25 to 7.0 GPa.

We thus hypothesize that the differences between the creep and stress relaxation behavior are closely associated with the crystal structure of the material, the corresponding available slip systems and the interactions between dislocations during nanoindentation. MAPbBr<sub>3</sub> at room temperature has a body-centered cubic (BCC) structure. It also has 48 possible slip systems (16 accessible during nanoindentation), which is the most out of all the materials that were tested. In comparison, KBr is also cubic but adopts a face-centered cubic (FCC) with only 12 possible slip systems. In addition to the number of slip systems available, the crystal structure dictates how dislocations will propagate during a nanoindentation experiment.

Figure 2e-f show the activated planes for representative FCC and a BCC crystals indented on the (100) plane. After nucleation in FCC crystals, the dislocations tend to move towards the central axis under the indenter, where the slip planes interact and become tangled, preventing their further propagation (Figure 2e).<sup>[25]</sup> This is consistent with our observations of KBr displaying the lowest creep and relaxation despite the low activation energy for slip.

During loading, multiple dislocations nucleate simultaneously in KBr; these dislocations are tangled early on and consequently their motion halted during subsequent creep or stress relaxation. The opposite is true for BCC cubic crystals (Figure 2f), where the dislocations are driven away from the indenter axis, making tangling of dislocations less probable.<sup>[25]</sup> These dislocations thus continue to propagate during creep and stress relaxation. It follows that, the stress relaxation data shown Figure 1d suggest that dislocation entanglement is more probable in the orthorhombic structure (CsPbBr<sub>3</sub>) than in the tetragonal structure (MAPbI<sub>3</sub>). Two-dimensional representations of slip propagation in both FCC and BCC crystal are shown in Figures S2c and S2d, respectively.

Figure 1c shows that MAPbI<sub>3</sub> and CsPbBr<sub>3</sub> exhibit very similar creep displacements. Although they adopt tetragonal and orthorhombic structures respectively, their lattice parameters are very similar (see Table S1). Both the tetragonal and orthorhombic structures can be thought of as elongated cubic structures; this elongation breaks the symmetry of the BCC unit cell and reduces the number of possible available slip systems. Although we do not know which slip systems are activated in the tetragonal and orthorhombic perovskite structures, we postulate that, due to their resemblance to the cubic phase, the dislocations are similar to that of the BCC cubic crystal. However, not all systems are activated because of the reduced symmetry.

The underlying mechanism for load relaxation is the same as creep. However, there is a delayed response from the material to the applied stress resulting from displacing the nanoindenter tip into the sample. While the displacement is kept constant, the material continues to deform, and as this deformation happens, the load decreases. From the previous discussion, we conclude that the onset of plasticity is governed by the onset of dislocation motion, while the creep and stress relaxation behavior is governed by the probability of the nucleated dislocations to propagate.

To understand the influence of deformation time scales on the plastic deformation, we performed creep and relaxation tests while loading at different rates across three orders of magnitude. We summarize the rate dependence of each material by plotting the total measured creep displacement and stress relaxation after 30 seconds in Figures 3a-b, respectively. Individual plots, corresponding to all the single crystals tested, are shown in Figure S4. All three perovskite single crystals exhibit a pronounced rate dependence, while the rate dependence of KBr is negligible in comparison.

All the samples exhibited an increased creep displacement, and stress relaxation as a function of increased loading or displacement rate, respectively. For creep tests at high loading rates, the strain gradient in the direction perpendicular to the surface tested is greater than that at low loading rates. The large strain gradient causes more dislocations to be nucleated during the loading step. These propagate and interact in the constant load/displacement regime. At low loading rates the strain gradient is lower, allowing for dislocations to nucleate, propagate and tangle with one another. The tangling of dislocations results in strain hardening during loading and small creep displacements/stress relaxation phenomena that occur during the constant load/displacement period.<sup>[19]</sup> MAPbBr<sub>3</sub> shows the largest rate-dependence of all materials, while KBr exhibits the lowest. This is consistent with the availability of slip systems in each crystal and the tendency of dislocations to move away or towards the indenter axis.

To better describe the viscoplastic properties of the tested materials and to quantify the differences between their time-dependent response, the creep and relaxation curves were fitted to an analytical expression extracted from a rheological model composed of springs and dashpots (Figure 1c-d).<sup>[26, 27]</sup> The fit of our model captures the behavior of all materials tested in both creep and stress relaxation experiments, allowing us to extract Young's and shear moduli values in addition to relaxation times (Table S2-S3). A detailed description of the model can be found in the Supporting Information.

In summary, we demonstrated that both HOIPs and IPs show large creep deformation, load relaxation, and a pronounced rate-dependent mechanical behavior relative to a model ionic crystal of KBr. We interpret this viscoplastic behavior for HOIPs and the inorganic CsPbBr<sub>3</sub>, to indicate that the organic cation plays little role in time- and rate-dependent plastic deformation, and that the Pb-X frame work is more important. By modeling the creep and relaxation behavior using rheological components we have the advantage of determining both the elastic and viscous characteristics of the specific perovskite single crystals in this study. It is expected for materials with crystals of low hardness to creep under the conditions utilized in the current study. During nanoindentation experiments, FCC crystals will creep less due to the dislocation movement towards the axis of the indenter tip and the reduced number of available slip systems. The present study has implications in the future study of the mechanical properties of perovskite single crystals, both hybrid and inorganic. The results provided will help the effective design of flexible perovskite devices since the low hardness and the viscoplastic properties demonstrated are not conducive to flexible applications. Moreover, the pronounced rate-dependent mechanical properties can significantly impact how these materials are processed in large scale. A comprehensive understanding of the impact of plastic deformation on the performance of HOIP-based photovoltaic devices is needed for their effective application in flexible structures.

### **Experimental Section**

*Crystal growth.* MAPbBr<sub>3</sub> and MAPbI<sub>3</sub> single crystals were grown by inverse temperature crystallization as reported by Saidaminov et al.<sup>[28]</sup> CsPbBr<sub>3</sub> crystals were synthesized by vertical Bridgman crystallization method published by Stoumpos et al.<sup>[16]</sup>

*Sample preparation.* All single crystals were glued (Loctite 495) to stainless steel atomic force microscopy specimen discs before nanoindentation experiments. No polishing

was performed on HOIPs samples. Polished and unpolished CsPbBr<sub>3</sub> crystals were tested and no significant difference in their mechanical response was observed.

*Equipment and settings.* Indentation experiments were performed using a TriboScope® Nanomechanical Testing System (Hysitron Inc., Minneapolis, MN). For creep and stress relaxation measurements a Berkovich indenter (three-sided pyramid shape tip) was used. A 3 μm-diameter cono-spherical tip was used to detect pop-in events. Creep experiments were conducted under load displacement with a maximum load of 2000 μN and loading rates of 10, 100 and 1000 μN s<sup>-1</sup>. Stress relaxation experiments were conducted under displacement control with a maximum displacement of 600 nm and displacement rates of 3, 30 and 300 nm s<sup>-1</sup>.

### Supporting Information

Supporting Information is available from the Wiley Online Library or from the author.

### Acknowledgements

This research was supported by MRM's appointment to the Intelligence Community Postdoctoral Research Fellowship Program at Princeton University, administered by Oak Ridge Institute for Science and Education through an interagency agreement between the U.S. Department of Energy and the Office of the Director of National Intelligence. YLL acknowledges the financial support from the National Science Foundation through grants ECCS-1549619 and CMMI-1537011. WOS acknowledges the World Bank for financial support. Work at Argonne National Laboratory was supported by the U.S. Department of Energy (DOE), Office of Science, Basic Energy Sciences (BES) under contract no. DE-AC02-06CH11357.

Received: ((will be filled in by the editorial staff))

Revised: ((will be filled in by the editorial staff))

Published online: ((will be filled in by the editorial staff))

### References

- [1] J. Berry, T. Buonassisi, D. a. Egger, G. Hodes, L. Kronik, Y.-L. Loo, I. Lubomirsky, S.

- R. Marder, Y. Mastai, J. S. Miller, D. B. Mitzi, Y. Paz, A. M. Rappe, I. Riess, B. Rybtchinski, O. Stafsudd, V. Stevanovic, M. F. Toney, D. Zitoun, A. Kahn, D. Ginley, D. Cahen, *Adv. Mater.* **2015**, *27*, 5101.
- [2] R. A. Jishi, O. B. Ta, A. A. Sharif, *J. Phys. Chem. C* **2014**, *118*, 28344.
- [3] M. A. Green, K. Emery, Y. Hishikawa, W. Warta, Ewan D. Dunlop, *Prog. Photovolt Res. Appl.* **2016**, *24*, 905.
- [4] M. Kulbak, D. Cahen, G. Hodes, *J. Phys. Chem. Lett.* **2015**, *6*, 2452.
- [5] R. Sheng, A. Ho-Baillie, S. Huang, S. Chen, X. Wen, X. Hao, M. A. Green, *J. Phys. Chem. C* **2015**, *119*, 3545.
- [6] A. Kojima, K. Teshima, Y. Shirai, T. Miyasaka, *J. Am. Chem. Soc.* **2009**, *131*, 6050.
- [7] M. Ibrahim Dar, M. Abdi-Jalebi, N. Arora, T. Moehl, M. Grätzel, M. K. Nazeeruddin, *Adv. Mater.* **2015**, *27*, 7221.
- [8] S. Yakunin, D. N. Dirin, Y. Shynkarenko, V. Morad, I. Cherniukh, O. Nazarenko, D. Kreil, T. Nauser, M. V. Kovalenko, *Nat. Photonics* **2016**, *10*, 1.
- [9] M. I. Saidaminov, M. A. Haque, M. Savoie, A. L. Abdelhady, N. Cho, I. Dursun, U. Buttner, E. Alarousu, T. Wu, O. M. Bakr, *Adv. Mater.* **2016**, 8144.
- [10] P. Docampo, J. M. Ball, M. Darwich, G. E. Eperon, H. J. Snaith, *Nat. Commun.* **2013**, *4*, 2761.
- [11] F. Brivio, J. M. Frost, J. M. Skelton, A. J. Jackson, O. J. Weber, M. T. Weller, A. R. Goñi, A. M. A. Leguy, P. R. F. Barnes, A. Walsh, *Phys. Rev. B* **2015**, *92*, 144308.
- [12] Y. Rakita, S. R. Cohen, N. K. Kedem, G. Hodes, D. Cahen, *MRS Commun.* **2015**, *3*, 1.
- [13] S. Sun, Y. Fang, G. Kieslich, T. J. White, A. K. Cheetham, *J. Mater. Chem. A* **2015**, *3*, 18450.
- [14] J. Feng, *APL Mater.* **2014**, *2*, 81801.
- [15] J. K. Galt, **1948**, *73*, 2.
- [16] C. C. Stoumpos, C. D. Malliakas, J. A. Peters, Z. Liu, M. Sebastian, J. Im, T. C. Chasapis, A. C. Wibowo, D. Y. Chung, A. J. Freeman, B. W. Wessels, M. G. Kanatzidis, *Cryst. Growth Des.* **2013**, *13*, 2722–2727.
- [17] L. Wang, H. Bei, T. L. Li, Y. F. Gao, E. P. George, T. G. Nieh, *Scr. Mater.* **2011**, *65*, 179.
- [18] S.-R. Jian, Y.-C. Tseng, I.-J. Teng, J.-Y. Juang, *Materials (Basel)*. **2013**, *6*, 4259.
- [19] S. A. Syed Asif, J. B. Pethica, *Philos. Mag. A* **1997**, *76*, 1105.
- [20] J. C. Tan, A. K. Cheetham, *Chem. Soc. Rev.* **2011**, *40*, 1059.
- [21] C. A. Schuh, *Mater. Today* **2006**, *9*, 32.

- [22] J. E. Bradby, J. S. Williams, M. V. Swain, *J. Mater. Res.* **2004**, *19*, 380.
- [23] F. R. N. Nabarro, *Mater. Sci. Eng. A* **2001**, *309–310*, 227.
- [24] B. Yang, L. Riester, T. G. Nieh, *Scr. Mater.* **2006**, *54*, 1277.
- [25] L. Wang, H. Bei, T. L. Li, Y. F. Gao, E. P. George, T. G. Nieh, *Scr. Mater.* **2011**, *65*, 179.
- [26] J. Mencik, L. H. He, J. Němeček, *Polym. Test.* **2011**, *30*, 101.
- [27] M. L. Oyen, *Philos. Mag.* **2006**, *86*, 5625.
- [28] M. I. Saidaminov, A. L. Abdelhady, B. Murali, E. Alarousu, V. M. Burlakov, W. Peng, I. Dursun, L. Wang, Y. He, G. Maculan, A. Goriely, T. Wu, O. F. Mohammed, O. M. Bakr, *Nat. Commun.* **2015**, *6*, 7586.

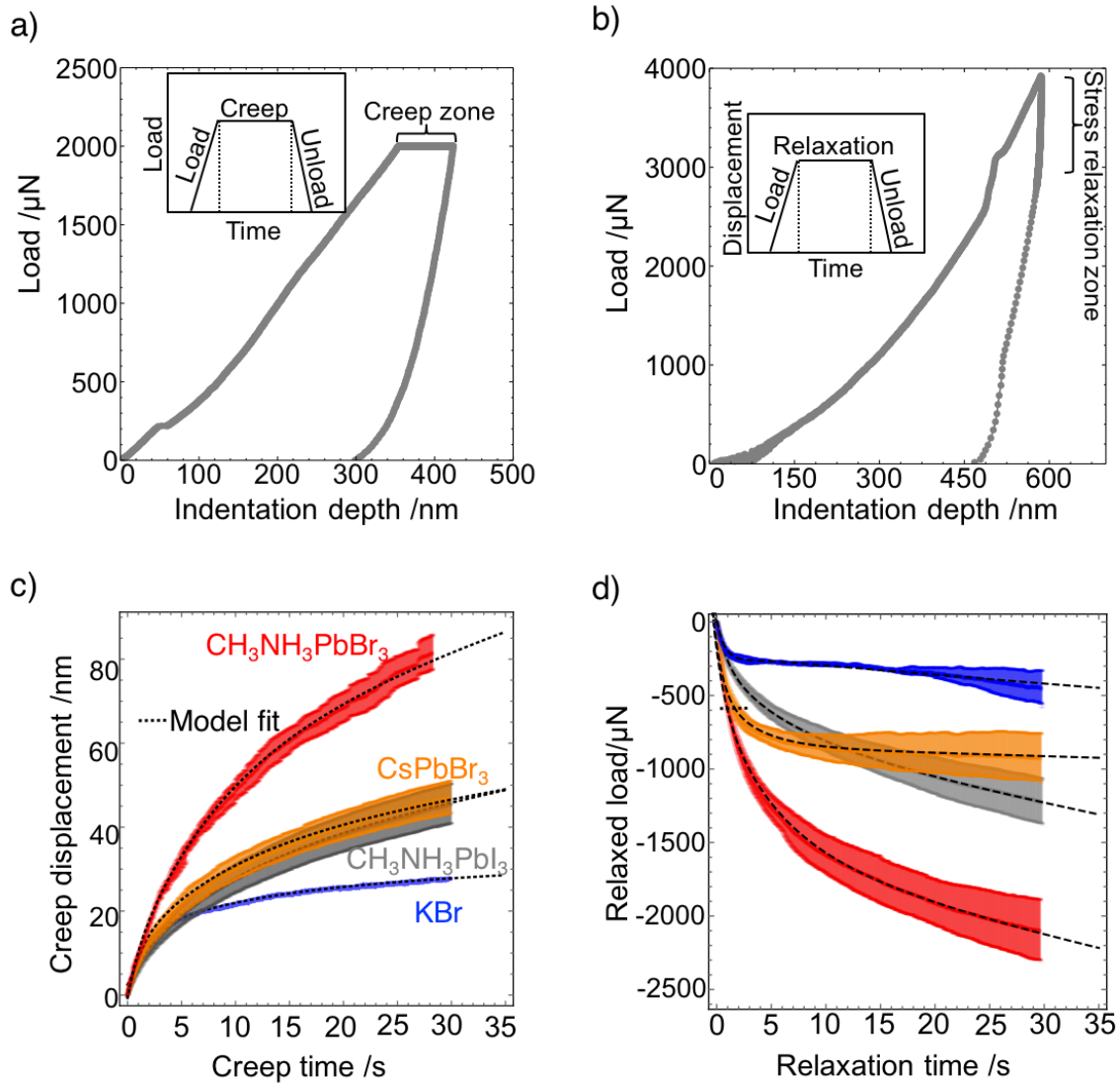


**Figure 1.** a) Representative load-indentation depth curve for load-controlled nanoindentation experiment on a MAPbI<sub>3</sub> single crystal. The load function in the inset displays loading, constant-load (creep) and unloading with time. The ramp time to maximum load was  $t_R = 20 \text{ s}$  and the maximum load was held at  $P_{max} = 2000 \mu\text{N}$  for 30 s in all creep experiments. b) Representative load-indentation depth curve for displacement-controlled nanoindentation experiment on the same MAPbI<sub>3</sub> single crystal. The displacement function in the inset displays loading, constant displacement holding (stress relaxation) and unloading with time. The ramp time to maximum displacement was  $t_R = 20 \text{ s}$  and the maximum displacement was held at  $d_{max} = 600 \text{ nm}$  for 30 s in all stress relaxation experiments. c) Creep displacement curves and d) Load relaxation curves for the four single crystals tested. Bands represent the

standard error extracted from three independent measurements on each single crystal. The fit of our viscoplastic model (dotted line) captures the behavior of all the single crystals tested in both creep and stress relaxation experiments.

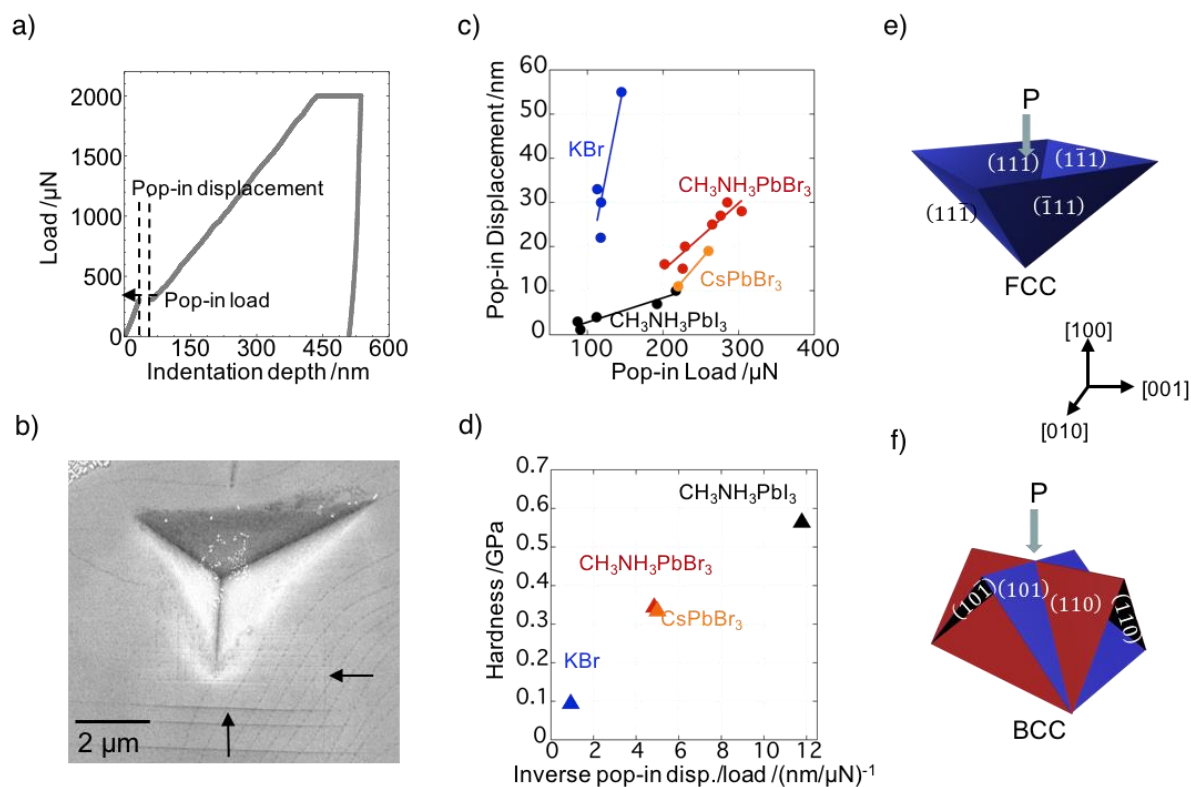


**Figure 2.** a) A pop-in event is captured during loading on a MAPbI<sub>3</sub> single crystal. The first pop-in event indicates the elastic-to-plastic transition. b) Scanning electron micrograph revealing slip-shear bands (highlighted with arrows) on the surface of MAPbBr<sub>3</sub> crystal as a result of plastic deformation during a nanoindentation experiment using a Berkovich indenter. Slip-shear bands are expected from the activation of slip systems in a BCC crystal. c) Measured pop-in displacement as a function of pop-in load for all single crystals tested. The inverse slope for each single crystal is related to the energy released during the initiation of slip dislocation. d) Relation between the hardness and the energy released as quantified by inverse of slopes in (c). Schemes illustrating slip-plane propagation under the indenter in e) FCC and f) BCC crystals. Of the slip planes available in BCC crystals, only the family of the most atomically dense planes, {110}, is shown. Indentation load (P) is on the (100) plane in

both cases. The slip planes in FCC (e) converge under the indenter axis. Slip planes in BCC (f) diverge from the indenter axis.

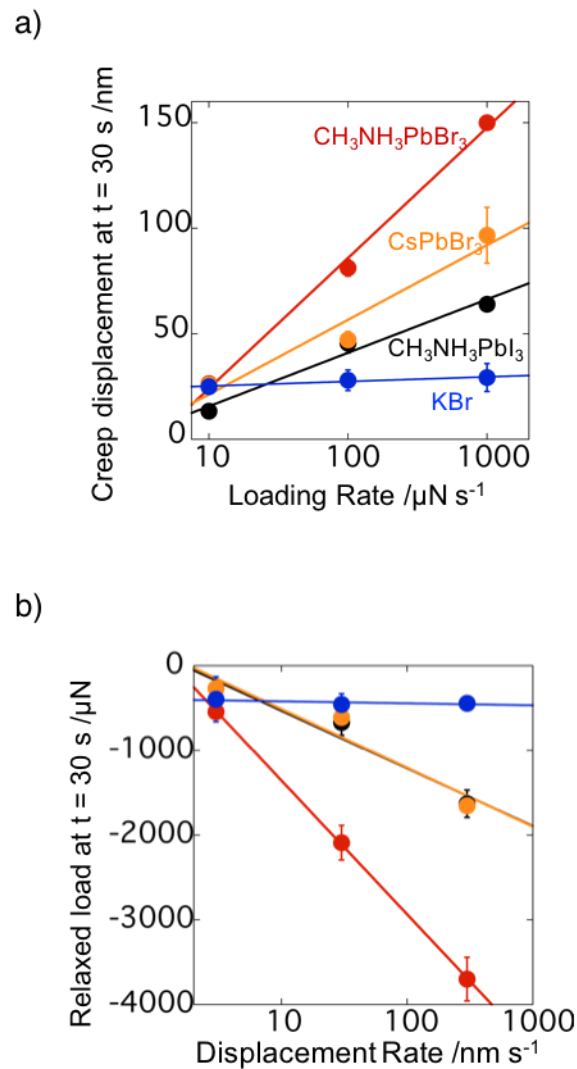


**Figure 3.** a) Measured loading rate dependence of creep and b) displacement rate dependence of stress relaxation. Each data point corresponds to the (a) creep displacement and (b) relaxed load at  $t = 30$  s during the constant load and displacement segments respectively. In both experiments the perovskite single crystals display a higher rate-dependence of creep and stress relaxation compared to the KBr single crystal. The solid lines are visual guides.

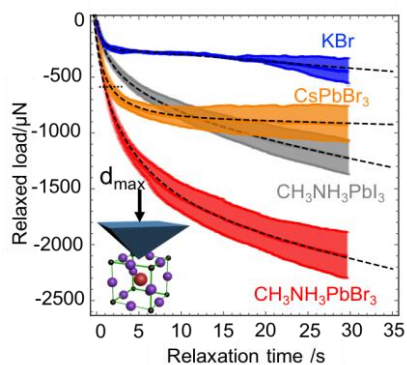
**Dynamic mechanical response of hybrid organic-inorganic and inorganic perovskite** crystals suggests that the time-dependent mechanical properties of lead-halide perovskites are independent of the chemical character of the A-site cation. Moreover, significant viscoplastic behavior is revealed through creep and stress relaxation measurements. These phenomena are interpreted as direct results of the crystal structures and how dislocations propagate within them.

### Perovskite dynamic mechanical properties

*Marcos A. Reyes-Martinez, Ahmed L. Abdelhady, Makhsud I. Saidaminov, Duck Young Chung, Osman M. Bakr, Mercuri G. Kanatzidis, Wole O. Soboyejo and Yueh-Lin Loo\**

### Time-dependent Elasto-plastic Behavior of Lead Halide Perovskite Single Crystals

ToC figure ((Please choose one size: 55 mm broad  $\times$  50 mm high or 110 mm broad  $\times$  20 mm high. Please do not use any other dimensions))



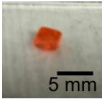
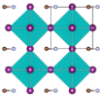
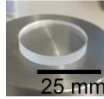
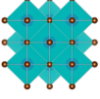
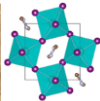
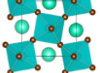
## Supporting Information

## Time-dependent elasto-plastic behavior of lead halide perovskite single crystals

Marcos A. Reyes-Martinez, Ahmed L. Abdelhady, Makhsud I. Saidaminov, Duck Young Chung, Osman M. Bakr, Mercuri G. Kanatzidis, Wole O. Soboyejo and Yueh-Lin Loo\*

## I. Structural parameters of single crystals tested

**Table S1.** Photographs, structural parameters and measured hardness for each single crystal tested.

Material	Structure	No. of slip systems	Lattice Constants [Å]	Hardness [GPa]
$\text{CH}_3\text{NH}_3\text{PbBr}_3$ P1  	Cubic (BCC)	48	$a = 6.59$	$0.36 \pm 0.03$
KBr Fm-3m  	Cubic (FCC)	12	$a = 5.93$	$0.15 \pm 0.5$
$\text{CH}_3\text{NH}_3\text{PbI}_3$ (Pnma)  	Tetragonal (BCC)	<48	$a = 8.85, c = 12.66$	$0.55 \pm 0.12$
$\text{CsPbBr}_3$ (Pnma)  	Orthorhombic (BCC)	<48	$a = 8.24, c = 11.73$	$0.34 \pm 0.02$

## II. CsPbBr<sub>3</sub> XRD

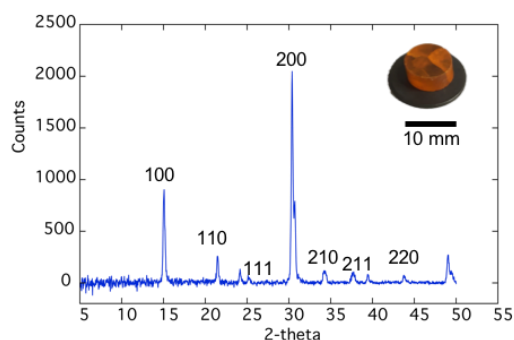


**Figure S1.** X-ray diffraction pattern of CsPbBr<sub>3</sub> crystal indicating preferential orientation normal to the (h00) plane.

## III. Slip systems and their interactions

Face-centered-cubic (FCC) crystals, such as KBr, have slip planes of the type  $\{111\}$  that slip in the  $\langle 110 \rangle$  direction. Body-centered-cubic (BCC) crystals, such as MAPbBr<sub>3</sub>, have three families of slip systems with planes of the type  $\{110\}$  with two  $\langle 111 \rangle$  directions,  $\{112\}$  and  $\{123\}$  each with one  $\langle 111 \rangle$  direction. Schemes illustrating these different slip systems in FCC and BCC crystals are shown in Figures S2a and S2b, respectively. Given the direction of the load applied by the nanoindenter tip and the crystal plane that we indented, we speculate that in KBr, with an FCC structure, its  $\{111\}$  planes and  $\langle \bar{1}10 \rangle$  directions are activated (Figure S2c).<sup>[1]</sup> For materials with BCC structure, slip systems with  $\{110\}$  planes and two  $\langle \bar{1}11 \rangle$  directions are mostly activated (Figure S2d). The BCC structure has other families of planes, but given that they are less atomically dense, they are less likely to be activated during nanoindentation.

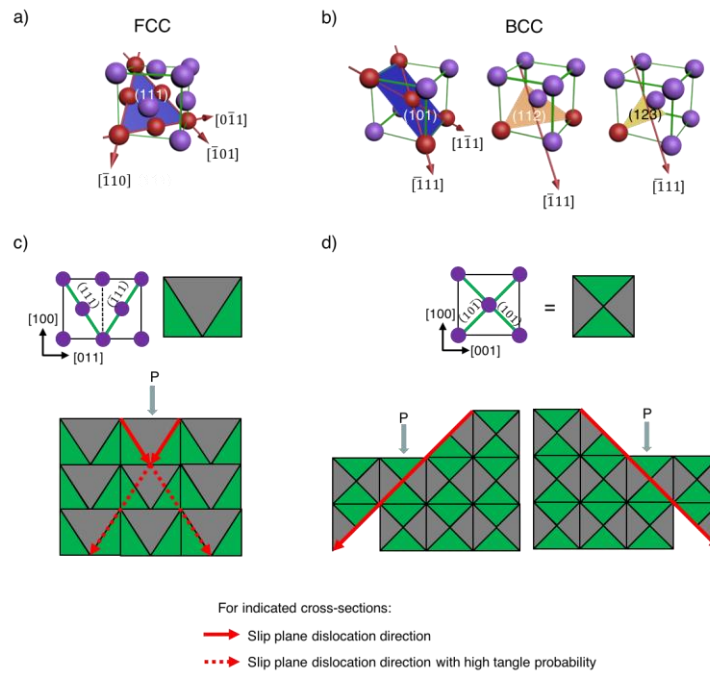


**Figure S2.** Slip planes and directions in a) FCC and b) BCC crystals. FCC crystals have 4 slip planes of the type  $\{111\}$ , each with 3 slip directions of the  $\langle \bar{1}10 \rangle$  type, totaling 12 slip systems. Of the 48 slip systems accessible in the BCC structure, 4 slip planes of the type  $\{110\}$  with two  $\langle \bar{1}11 \rangle$  directions, 4 slip planes of the type  $\{112\}$  and 4 slip planes of the type  $\{123\}$  each with one  $\langle 111 \rangle$  direction, totaling 16 systems, are accessible during nanoindentation. A two-dimensional representation of slip-plane propagation during nanoindentation in c) FCC crystals and d) BCC crystal.

## IV. Evidence of strain hardening

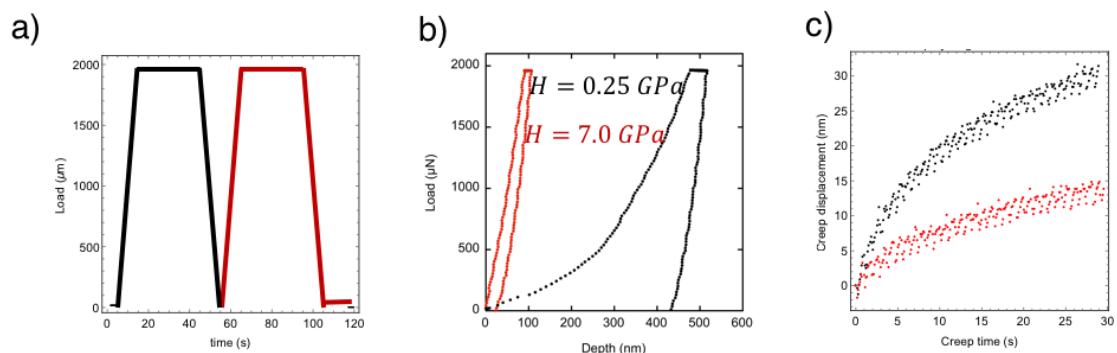


**Figure S3.** The MAPbI<sub>3</sub> single crystal underwent the same experiment twice on the same indentation area with a) loading history and b) the corresponding load-displacement curves. The second measurement (red) was shifted to the origin in (b) for ease of comparison. Corresponding hardness values ( $H$ ) is indicated in b). c) Creep displacements from the first cycle (black) and second cycle (red). A significant reduction in creep displacement is observed for the second measurement, indicating an increased resistance to plastic deformation. This observation is consistent with strain hardening.

V. Load/displacement rate dependence prediction of creep and stress relaxation curves

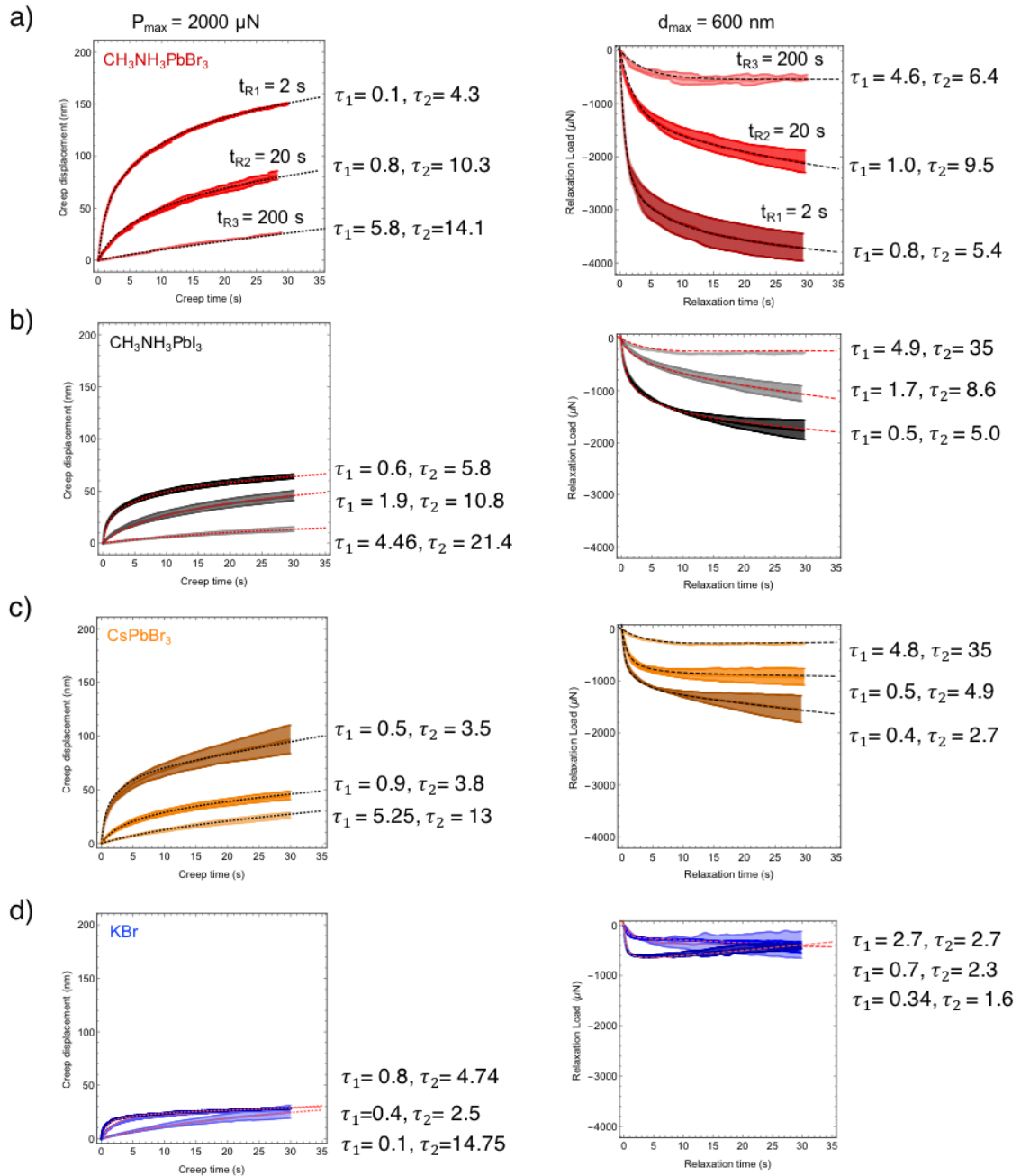
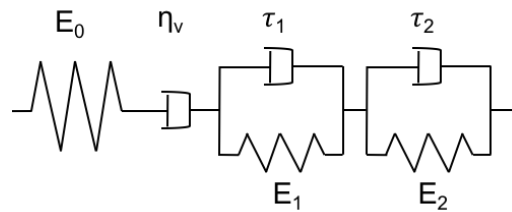


**Figure S4.** Experimental creep (left column) and stress relaxation (right column) curves corresponding to a)  $\text{MAPbBr}_3$ , b)  $\text{MAPbI}_3$ , c)  $\text{MAPbI}_3$  and d)  $\text{KBr}$  at ramp times  $t_R = 2, 20$  and  $200 \text{ s}$ . Bands represent the standard error extracted from three independent measurements on each single crystal. Dotted lines represent the fits for each individual  $t_R$ . The fitted characteristic times  $\tau_j$  for each experiment is shown.

## VI. Modeling of creep, stress-relaxation and rate dependence using rheological elements

The rheological model used (Scheme 1) includes a spring to capture the instantaneous elastic behavior in series with a dashpot to capture plastic slip. The spring connected in series to a dashpot, also known as a Maxwell element, captures stress relaxation. In addition, two Kelvin-Voigt components are also connected in series to capture creep.<sup>[2]</sup> The utilization of two Kelvin-Voigt components is empirical, based on the components providing the closest fit for all creep and relaxation data acquired in this study. Therefore, we do not attribute any correlation between rheological components in our model and physical components in the corresponding crystal structures.



**Scheme S1.** Rheological model that describes the viscoplastic behavior of the single crystals tested. The model includes an instantaneous elastic contribution,  $E_0$ , a viscous component  $\eta_v$ , and two Kelvin-Voigt components, composed of moduli  $E_1$ ,  $E_2$  and characteristic relaxation times  $\tau_1$  and  $\tau_2$  connected in series.

First, we approach stress relaxation experiments with the goal of obtaining an expression connecting load to time for a fixed displacement. An analytical expression corresponding to the rheological model in Scheme 1 can be written by considering the elastic relation between load ( $P$ ) and displacement ( $h$ ) from classical contact mechanics.<sup>[3]</sup>

$$P = K \frac{E}{1-\nu^2} h^m, \quad (1)$$

where  $E$  is the Young's modulus,  $\nu$  is the Poisson's ratio and  $K$  and  $m$  are geometric factors corresponding the shape of the indenter. For the pyramidal Berkovich indenter  $K = 2 \tan \beta / \pi$ , where  $\beta$  is half the angle of the indenter tip and  $m = 2$ . The Poisson's ratios for  $\text{MAPbBr}_3$  and  $\text{MAPbI}_3$  were reported by Feng<sup>[4]</sup> to be 0.29 and 0.33, while Cahen and coworkers<sup>[5]</sup> estimated it to be 0.33 for  $\text{CsPbBr}_3$ . Therefore, for simplicity we utilize  $\nu = 1/3$  in our calculations.

Using the relation  $E = 2G(1 + \nu)$ , Equation 1 is simplified to

$$P = Kh^2 3G. \quad (2)$$

For  $\text{KBr}$ , we utilize a Poisson's ratio of 0.138 from the literature.<sup>[6]</sup> To include the effects of ramp time (loading or displacement rate) we substitute the shear modulus  $G$  in Equation 2 by an integral operator equivalent to the stress relaxation function  $G(t)$  corresponding to our rheological model (additional details are provided in Supplementary Information):

$$P(t) = K \int_0^t G(t - t') \left( \frac{d\{h(t')\}^2}{dt'} \right) dt' \quad (3)$$

Solving this integral for the appropriate time boundaries for the ramp and hold periods we obtain the final expression for  $P(t)$  during stress relaxation:

$$P(t) = Kh_{max}^2 \left[ \sum C_j \rho_j \exp\left(-\frac{t}{\tau_j}\right) \right], \quad (4)$$

where  $h_{max}$  is the maximum displacement, held constant during stress relaxation period.  $C_j$  and  $\tau_j$  are the compliance and characteristic relaxation times for the springs and the dashpots

in the rheological model, respectively.  $\rho_j = \frac{2\tau_j}{t_R^2} \left[ \exp\left(\frac{t_R}{\tau_j}\right) (t_R - \tau_j) + \tau_j \right]$  is the ramp correction factor,<sup>[7]</sup> where  $t_R$  is the ramp time, defined as the time period to reach  $h_{max}$ .

For creep experiments, the analysis is analogous to the one outlined for stress relaxation. First we re-write Equation 2 with the goal of extracting an expression connecting displacement ( $h$ ) to time ( $t$ ) while holding the load ( $P$ ) fixed.

$$h^2 = \frac{1}{K3G} P. \quad (5)$$

We substitute the shear modulus in Equation 5 by an integral operator equivalent to the creep displacement function  $J(t)$  corresponding to our rheological model (additional details are provided in Supplementary Information). After solving the integral for the appropriate time boundaries for the ramp and hold periods we obtain the final expression:

$$h^2(t) = \frac{P_{max}}{K} \left\{ C_0 + C_v \left( t - \frac{t_R}{2} \right) + \sum C_j \left[ 1 - \rho_j e^{-t/\tau_j} \right] \right\}, \quad (6)$$

where  $C_0$  is the instantaneous compliance,  $C_v = 1/\eta$  is the viscous compliance and  $C_j$  is the instantaneous compliance of Kelvin-Voigt elements.  $\rho_j = \frac{\tau_j}{t_R} \left[ \exp\left(\frac{t_R}{\tau_j}\right) - 1 \right]$  is the ramp correction factor,<sup>[2,7]</sup> and  $t_R$  is the ramp time, defined as the time period the nanoindenter tip takes to reach  $h_{max}$ . Equations 4 and 6 can be used to fit the experimental data obtained from stress relaxation and creep, respectively. As can be seen from the fits (dotted lines) in Figures 2c and 2d, they capture the behavior of experimentally measured creep and load relaxation. From the fits, we can extract static mechanical properties, such as elastic, and shear moduli, in addition to the dynamic mechanical properties in the form of characteristic time constants,  $\tau_j$ . A summary of the values obtained in this study with those found in the literature is presented

in Table S2. Values of static properties are in qualitative agreement with the measured and estimated values of elastic modulus and shear modulus. In addition, the values obtained from fitting the creep data are like those obtained from fitting the load relaxation data, demonstrating the self-consistency of the model. Characteristic time constants corresponding to  $t_R = 20$  s are shown in Table S3.

**Table S2.** Young's modulus (E) and shear modulus (G) obtained from the Olive and Pharr nanoindentation method, from fits to the creep and stress relaxation experiments, compared to DFT calculations from the literature.

Material	E (100) [GPa]				G [GPa]		
	Olive and Pharr	Creep	Relax	DFT*	Creep	Relax	DFT*
CH <sub>3</sub> NH <sub>3</sub> PbBr <sub>3</sub> (100)	21.4 ± 4.0	28.0	23.7	22.6	10.5	8.9	10.4
KBr (100)	33.0 ± 4.1	30.4	31.6	-	13.3	13.9	-
CH <sub>3</sub> NH <sub>3</sub> PbI <sub>3</sub> (100)	10.8 ± 2.7	10.9	9.5	12.2	4.1	3.6	3.7
CsPbBr <sub>3</sub> (200)	11.3 ± 3.2	13.1	17.5	-	4.9	6.6	-

\*Values extracted from Ref. 14.

We utilized our model to fit all the experiments at all ramp times,  $t_R = 2, 20$  and  $200$  s (Figure S4). We observe that the characteristic time constants,  $\tau_j$ , change with loading rate. This observation is consistent with the qualitative change in the shape observed in both creep and relaxation curves as a function of rate. The behavior of the curve over time is captured by a change in the dynamic compliance which is related to viscosity through the expression  $\tau_j = C_j \eta_j$ . Our results indicate that the flow of material during plastic deformation is higher at higher rates, displaying lower viscosity. This behavior is phenomenologically analogous to the shear thinning in polymeric materials. Characteristic times can be used to quantify the differences in the relaxation behavior between CsPbBr<sub>3</sub> and MAPbI<sub>3</sub> (Figure 1d). For CsPbBr<sub>3</sub>,  $\tau_1$  and  $\tau_2$  have values of 0.5 and 4.9 s while for MAPbI<sub>3</sub> the values are 1.7 and 8.6 s. The lower  $\tau_j$  values for CsPbBr<sub>3</sub> are evidence of an earlier shift in the flow dynamics during nanoindentation that prevent it from relaxing further after 4.9 s.

**Table S3.** Characteristic relaxation times extracted from fits to the experimental creep and relaxation data at  $t_R = 20$  s.

Material	Creep [s]		Relaxation [s]	
	$\tau_1$	$\tau_2$	$\tau_1$	$\tau_2$
CH <sub>3</sub> NH <sub>3</sub> PbBr <sub>3</sub> (100)	0.8	10.3	1.0	9.5
KBr (100)	0.4	2.5	0.7	2.3
CH <sub>3</sub> NH <sub>3</sub> PbI <sub>3</sub> (100)	1.9	10.8	1.7	8.6
CsPbBr <sub>3</sub> (220)	0.9	3.8	0.5	4.9

## References

- [1] L. Wang, H. Bei, T. L. Li, Y. F. Gao, E. P. George, T. G. Nieh, *Scr. Mater.* **2011**, *65*, 179.
- [2] J. Mencik, L. H. He, J. Němeček, *Polym. Test.* **2011**, *30*, 101.
- [3] S. Shimizu, T. Yanagimoto, M. Sakai, *J. Mater. Res.* **1999**, *14*, 4075.
- [4] J. Feng, *APL Mater.* **2014**, *2*, 81801.
- [5] Y. Rakita, S. R. Cohen, N. K. Kedem, G. Hodes, D. Cahen, *MRS Commun.* **2015**, *3*, 1.
- [6] D. B. Sirdeshmukh, K. G. Subhadra, K. Kishan Rao, T. Thirimal Rao, *Cryst. Res. Technol.* **1995**, *30*, 861.
- [7] M. L. Oyen, *Philos. Mag.* **2006**, *86*, 5625.